Chinese Chemical Letters 32 (2021) 2073–2078

Contents lists available at ScienceDirect

Chinese Chemical Letters

journal homepage: www.elsevier.com/locate/cclet

Communication

Boron-iron nanochains for selective electrocatalytic reduction of nitrate

Fanfan Ni[a], Yuanyuan Ma[a], Junliang Chen[a], Wei Luo[a,b,*], Jianping Yang[a,b,*]

[a] State Key Laboratory for Modification of Chemical Fibers and Polymer Materials, College of Materials Science and Engineering, Donghua University, Shanghai 201620, China
[b] Institute of Functional Materials, Donghua University, Shanghai 201620, China

ARTICLE INFO

Article history:
Received 28 February 2020
Received in revised form 11 March 2021
Accepted 12 March 2021
Available online 18 March 2021

Keywords:
Nanostructured iron
Boron doping
Nitrate reduction reaction
Electrocatalysis

ABSTRACT

The electrocatalysis of nitrate reduction reaction (NRR) has been considered to be a promising nitrate removal technology. Developing a highly effective iron-based electrocatalyst is an essential challenge for NRR. Herein, boron-iron nanochains (B-Fe NCs) as efficient NRR catalysts were prepared *via* a facile low-cost and scalable method. The Fe/B ratio of the B-Fe NCs-x can be elaborately adjusted to optimize the NRR catalytic performance. Due to the electron transfer from boron to metal, the metal-metal bonds are weakened and the electron density near the metal atom centers are rearranged, which are favor of the conversion from NO_3^- into N_2. Moreover, the well-crosslinked chain-like architectures benefit the mass/electron transport to boost the exposure of abundant catalytic active sites. Laboratory experiments demonstrated that the optimized B-Fe NCs catalyst exhibits superior intrinsic electrocatalytic NRR activity of high nitrate conversion (~80%), ultrahigh nitrogen selectivity (~99%) and excellent long-term reactivity in the mixed electrolyte system (0.02 mol/L NaCl and 0.02 mol/L Na_2SO_4 mixed electrolyte), and the electrocatalytic activity of the material shows poor performance at low chloride ion concentration (Nitrate conversion of ~61% and nitrogen selectivity of ~57% in 0.005 mol/L NaCl and 0.035 mol/L Na_2SO_4 mixed electrolyte). This study provides a broad application prospect for further exploring the high-efficiency and low-cost iron-based functional nanostructures for electrocatalytic nitrate reduction.

Anthropogenic activities such as overfertilization, fossil fuel combustion and wastewater discharge lead to omnipresent surges of nitrogen in groundwater and surface water, which leads to an increasingly unbalanced global nitrogen cycle [1,2]. The imbalance of the nitrogen cycle has resulted in serious nitrate pollution in water resources, which is a menace to public health and ecosystems [3–5]. So far, various technologies have been reported to remove nitrate from wastewater, including biological process, physical approaches, and chemical reduction. Biological denitrification [6] is the most widespread technology, but it exists the technical problems of sludge production, high demand for conditions, and continuous monitoring. Physical approaches, such as ion exchange [7], electrodialysis [8] and reverse osmosis [9] can effectively remove the nitrate, but it will generate a large amount concentrated nitrate brine and need further treatment. Although chemical reduction process [10] can gain high removal rate of nitrate, the continuous addition of reducing agent (H_2) leads to a tedious process. Ideally, electrocatalytic nitrate reduction driven by renewable resources is a promising state-of-the-art technology to overcome these limitations. Therefore, this is a field worthy of further study [11–14]. It is remarkable that most of the electrocatalytic reactions rely heavily on the improvement of electrocatalysts with outstanding activity and stability [15–17]. According to previous catalytic studies, noble metals (*e.g.*, Rh, Ag, Pd) and their bimetallic systems (*e.g.*, PdAu, PdCu) have been considered to be excellent catalysts for nitrate reduction reaction (NRR) [18–21]. However, the high price and scarcity of precious metals limit the large-scale practical applications [19,22]. Therefore, a large number of researchers are committed to developing low-cost, corrosion-resistant, long-life electrodes aiming to purify nitrate-containing water as well as avoid the introduction of extra pollutants [23,24].

Nanoscale zero-valent iron is considered as the best promoter for NRR owing to its low price and relatively excellent electrocatalytic activity [25–28]. The electrocatalytic reaction occurs on the surface of the catalysts, making surface engineering a

* Corresponding authors at: State Key Laboratory for Modification of Chemical Fibers and Polymer Materials, College of Materials Science and Engineering, Donghua University, Shanghai 201620, China.
E-mail addresses: wluo@dhu.edu.cn (W. Luo), jianpingyang@dhu.edu.cn (J. Yang).

https://doi.org/10.1016/j.cclet.2021.03.042
1001-8417/

promising route to enhance the intrinsic activity of the nanoscale catalysts [29]. Through morphology engineering, the exposed surface active sites and selective facets can be regulated to increase the direct contact between the surface active sites and the catalytic substrate [30]. Su *et al.* reported self-assembly of Fe_3O_4 nanoparticle constitutional unit to constructed corchorifolius-like Fe@C microspheres consisting superlattice iron nanoparticles with rough surface, which can effectively facilitate the transformation of adsorbed nitrate into nitrite [25]. Lan *et al.* proposed a facile strategy to synthesize one-dimensional carbon nanofiber architecture equipped with Fe/Fe_3C nanoparticles immobilized on monodisperse carbon matrix through confined reduction. The cross-linked network structure increases the contact area between the electrolyte and the catalyst surface [26]. The utilization of active ingredients can be improved by manipulating the interface morphology. Another effective strategy is to introduce another additive into the host nanostructure, which can not only integrate the properties of the two materials, but also entrust the catalysts with new functions owing to the existence of abundant interfaces [27,31]. Wang *et al.* designed nitride-carbon encapsulated N-doped iron (FeN-NC) nanostructure with the assistant of hydrothermal treatment combined with pyrolysis. N dopants and NC shell promote mass and electron transfer from FeN to nitrogen for improving nitrogen selectivity [27]. Although some electrocatalysts have been developed for boosting the performance of NRR, most of them are concerned on the surface coating or matrix dispersion of carbon on nanostructured iron. It is still rarely involved the interfacial design of nanostructured iron for NRR. In this respect, Jiao *et al.* developed boron-doped Fe-N-C (FeBNC) single-atom nanozymes (SAzymes) *via* one-pot pyrolysis process. Boron dopants induce electronic structure rearrangement of the central Fe atom, further reducing the energy barrier for formation of hydroxyl radical (OH^*) to boost peroxidase-like activity [32]. Therefore, the surface modification of nanostructured iron makes the catalysts represent satisfactory continuous catalytic activity [5,33–35].

Herein, inspired by boron doping-iron nanostructures, a novel boron-iron nanochains was prepared with a simple wet-chemical process using sodium borohydride and ferric chloride as precursors. The B-Fe NCs nanostructures exhibit tunable elements ratio (B/Fe), uniform diameters (~60 nm), and nanochain morphology. The designed B-Fe NCs catalyst with suitable B/Fe ratio shows excellent electrocatalytic activity and stability for NRR along with a high nitrate conversion of ~80% and good selectivity for nitrogen of ~99%.

A schematic fabrication process of the B-Fe NCs-x catalysts was illustrated in Fig. 1a, $NaBH_4$ could easily reduce metal cations and form metal borides under the condition of frozen water [36]. The pH monitoring diagram of reaction solution during material preparation was shown in Fig. 1b. The pH value of sodium borohydride solution was alkaline (~9.28) and increased rapidly at the beginning of the reaction. With the increase of reaction time, the pH value of solution emerged an increasing trend (the pH is 10.34 at the end of the reaction) (Fig. 1b). In the later period of the reaction, the increase of pH value tended to be gentle. This visually illustrates the changing process of the reaction rate from drastic to slow. Then, a series of B-Fe NCs-x with different Fe loadings were constructed by adjusting the amount of $FeCl_3{\cdot}6H_2O$. We found that the B-Fe NCs catalyst prepared with a $FeCl_3$ and $NaBH_4$ molar ratio of 0.15:5 possessed the highest NRR property. Therefore, the B-Fe NCs catalyst discussed below were prepared under this condition unless otherwise specified.

The detailed morphological and structural features of the B-Fe NCs were first characterized by scanning electron microscopy (SEM) and transmission electron microscopy (TEM), as shown in Figs. 1c-e. The B-Fe NCs catalyst remains well-crosslinked chain-like architectures (Figs. 1d and e) with diameters around 60 nm and iron oxide shell thicknesses of about 5 nm (Fig. 1e). This oxide layer is generally considered to protect the iron core from rapid oxidation in the air, which makes the formed nanochains thermodynamically stable [37]. Furthermore, the morphologies of other Fe/B ratios catalysts (B-Fe NCs-x) also display well-crosslinked chain-like architectures (Figs. S1a-d in Supporting information). The well-crosslinked chain-like architectures is conducive to mass/electron transfer [38]. For comparison, the catalyst without B doped (named as Fe NPs) was prepared by replacing $NaBH_4$ with hydrazine hydrate. The non-boron-doped Fe is composed of iron nanoparticles with 50–100 nm (Fig. S1e in Supporting information). The lattice fringe of B-Fe NCs is 0.4934 nm, corresponding to the (220) plane of cubic Fe (Fig. 1e). The scanning transmission electron microscopy (STEM) elemental mappings (Figs. 1f-i) illustrate the homogeneous distribution of Fe, B and O in confinement framework of iron oxide shell. The energy dispersive X-ray spectroscopy (EDX) spectra (Fig. 1j) also confirms the presence of the three elements.

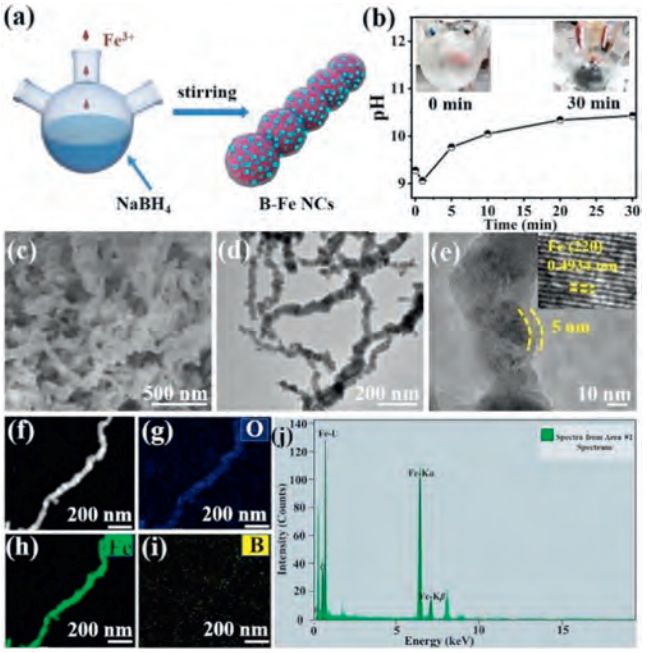

Fig. 1. (a) A schematic fabrication process of the B-Fe NCs-x. (b) The pH values of solution changes with reaction time after adding $FeCl_3$ aqueous solution into sodium borohydride aqueous solution (inset are optical Photographs of B-Fe NCs catalyst preparation process for 0 min and 30 min). (c) SEM, (d)-(e) TEM images of the B-Fe NCs (inset is HRTEM image in panel (e)). (f)-(i) STEM elemental mapping images, and (j) the corresponding EDX spectra of B-Fe NCs.

Moreover, the inductively coupled plasma (ICP) also confirms the presence of B in B-Fe NCs-x samples and determines the contents of iron, oxygen and boron in samples (Table S1 in Supporting information), showing that B-Fe NCs catalyst contains the highest iron content of ~86.53 wt%. The increasing content of iron can promote the active sites exposure and enhance the electrocatalytic activity of samples [25]. It is worth noting that the content of boron in B-Fe NCs-x does not increase with the increase of iron content. Therefore, the appropriate content of boron can optimize the interface of nanostructured iron and further improve their NRR performance. In addition, ICP test also shows that the iron content of boron-free sample is ~91.98 wt%, which is consistent with the result (~95.02 wt%) of thermogravimetric analyzer (TGA) (Fig. S2 in Supporting information).

X-ray diffraction (XRD) patterns display that the three typical diffraction peaks of cubic phase zero-valent iron (PDF # 06−0696)

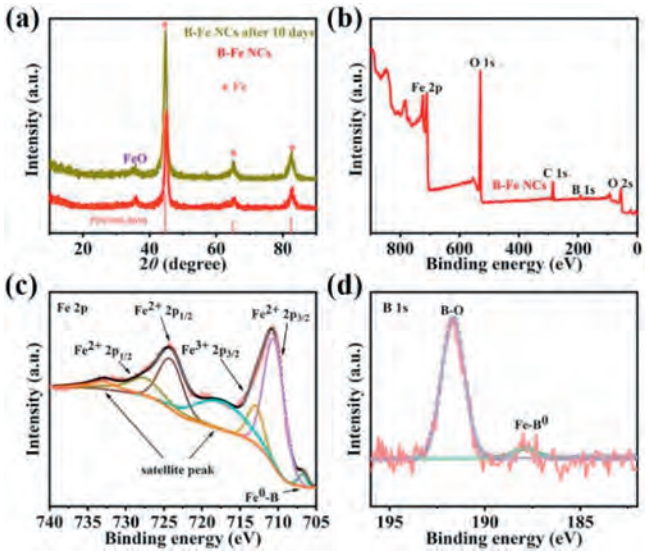

Fig. 2. Characterizations of B-Fe NCs. (a) XRD patterns. (b) XPS survey spectra. (c) High-resolution Fe 2p XPS spectra, and (d) high-resolution B 1s XPS spectra of B-Fe NCs.

can be observed (Fig. 2a and Fig. S3a in Supporting information). In addition, a weak peak of FeO can be observed due to the oxidation of Fe in air, which is consistent with the TEM images. Besides, the B-Fe NCs is still chemically stable after stored in argon atmosphere for ten days (green line in Fig. 2a). The surface chemical composition and electronic structure of different samples were analyzed by X-ray photoelectron spectroscopy (XPS) (Fig. 2b and Fig. S3b in Supporting information), indicating the presence of B, O, and Fe in B-Fe NCs-x catalysts. The high-resolution Fe 2p spectrum (Fig. 2c, Figs. S3c, S4a, S4c, S5a and S5c in Supporting information) matched well with two spin-orbit at 710 eV and 724 eV of Fe $2p_{3/2}$ and Fe $2p_{1/2}$,with satellite peaks at 717.6 and 732.7 eV [39]. Notice that the Fe $2p_{3/2}$ binding energy of the B-Fe NCs is negatively shifted by 0.5 eV relative to the binding energy of pure iron (710.7 eV), and the peaks could be decomposed into the Fe^{2+} peaks at 717.6 eV and 732.7 eV, and Fe^{3+} peaks at 713.6 eV and 724.9 eV, respectively. During the XPS test process, the Fe atoms exposed to the outermost layer would be inevitably oxidized to a high valence state in a trace amount. The high-resolution B 1s spectrum (Fig. 2d) of the B-Fe NCs could be assigned to two peaks, matching with the interaction between boron and residual iron at 188.8 eV and the boron-oxides species at 191.6 eV, respectively [40]. The B 1s binding energy is positively shifted by 1.7 eV relative to the binding energy of boron (187.1 eV) [41]. Other high-resolution B 1s spectrum of the B-Fe NCs-x samples can also be observed (Figs. S3d, S4b, S4d, and S5b in Supporting information). Furthermore, the boron peak of Fe NPs cannot be observed in the high-resolution B 1s spectra (Fig. S5d in Supporting information). The results indicate that due to the electron transfer from boron to metal, the metal-metal bonds are weakened and the electron density near the metal atom centers are rearranged [33,41–43]. In conclusion, XPS results not only demonstrate the coexistence of Fe, B and O, but also confirm the existence metal—B bond, metal—O bond, and B—O bond, which may further rearrange the electronic distribution of elements.

A series of catalysts were used to evaluate the denitrification performance under different conditions (different electrolyte types, reaction time and different NO_3^--N concentration), as shown in Fig. 3. When the electrolysis test run for 24 h, nitrate conversion and nitrogen selectivity of all cathodes can be observed in Fig. 3a. The results show that B-Fe NCs possesses highest nitrate removal (65%) and N_2 selectivity (95%), this phenomenon indicates that the appropriate Fe/B ratio improves the NRR performance greatly. Compared with boron-free sample (Fe NPs), the metal borides have significantly increased the activity of NRR. For one thing, the doped boron atoms not only manipulate the electronic structure of iron and largely enhance the transfer of electrons, but also improve the adsorption capacity of nitrate. For another, the compound heterointerfaces between oxide layer and iron in B-Fe NCs-x expose more active sites to activate the adsorption property of reaction intermediates [43]. In addition, the effect of dissolved oxygen in the reaction solution on the catalyst can be investigated in Fig. 3b. The deionized water used in this research was treated with argon or without any further processing. The final conversion of nitrate enhanced from 65% to 70% with removal of dissolved oxygen in deionized water during material preparation, reducing the uncontrolled oxidation of iron nanoparticles. However, there is no effect improvement for nitrogen selectivity. Subsequently, the influence of the electrolyte style was further evaluated to study the catalytic performance of NRR (Fig. 3b). A lot of experiments on iron-based materials show that the appropriate increase of electrolyte concentration could promote the performance of catalysts [25,26,44]. The results show that the nitrate conversion reaches 80% and the nitrogen selectivity reaches 99% after 24 h in mixed electrolyte type (0.02 mol/L NaCl and 0.02 mol/L Na_2SO_4 electrolyte). The increase of concentration is beneficial to the nitrate conversion and nitrogen selectivity. Therefore, the subsequent performance tests were completed in the mixed system.

In fact, the nitrate conversion could reach 96%, and the nitrogen selectivity could approach 100% with the prolongation of electrolysis time (36 h) in mixed electrolyte type containing 100 mg/L NO_3^--N (Fig. 3c). The B-Fe NCs cathode was used to determine the evolution of nitrate, nitrite, ammonia and nitrogen with reaction time during the electrolysis. When the electrolysis test increases from 6 h to 36 h, the removal rate of nitrate concentration gradually increased, from 53% at the beginning of 6 h to 96% after 36 h reaction. It is worth noting that the content of nitrite can be ignored. Nitrate concentration gradually decreases, and the reduction products are mainly ammonium and nitrogen. The contents of ammonia increase to the maximum about 6 h at the beginning and then decrease below ~1%. The nitrogen content is almost zero at the beginning and finally reach ~99.57%. In addition, the reduction products of the comparative sample (Fe NPs) change with times as shown in Fig. S6 (Supporting information), which electrocatalytic activity also shows an increasing trend with the prolongation of time. It is worth noting that the nitrogen selectivity (12%) could not be ignored in the first 6 h of the reaction. The previous research reports shown that the target product of nitrate reduction by nano-zero-valent iron is nitrogen, but our experimental results show that the main product in the initial stage of reaction is ammonium, and then ammonium is converted into nitrogen based on the breakpoint chlorination reaction [45]. This experimental phenomenon is obviously different from zero-valent iron, so it can be inferred that the catalytic active site is B-Fe [46,47]. The profound mechanism of this interesting phenomenon deserves further investigation.

It is essential to investigate the influence of different molarity ratios of Cl^- and SO_4^{2-} on electrocatalytic activity in mixed electrolyte system (NaCl and Na_2SO_4) [26]. As shown in Fig. 3b and Fig. S7a (Supporting information), obviously, the reduction of Cl^- (0.005 mol/L, 0.01 mol/L and 0.02 mol/L) results in a significant decrease in nitrate removal, and the corresponding selectivity of nitrogen also decreases markedly. The results indicate that a higher Cl^- concentration is propitious to the generation of nitrogen while a higher SO_4^{2-} concentration is beneficial to the conversion of nitrate into ammonia in mixed electrolyte system. Based on the comprehensive consideration of electrocatalytic

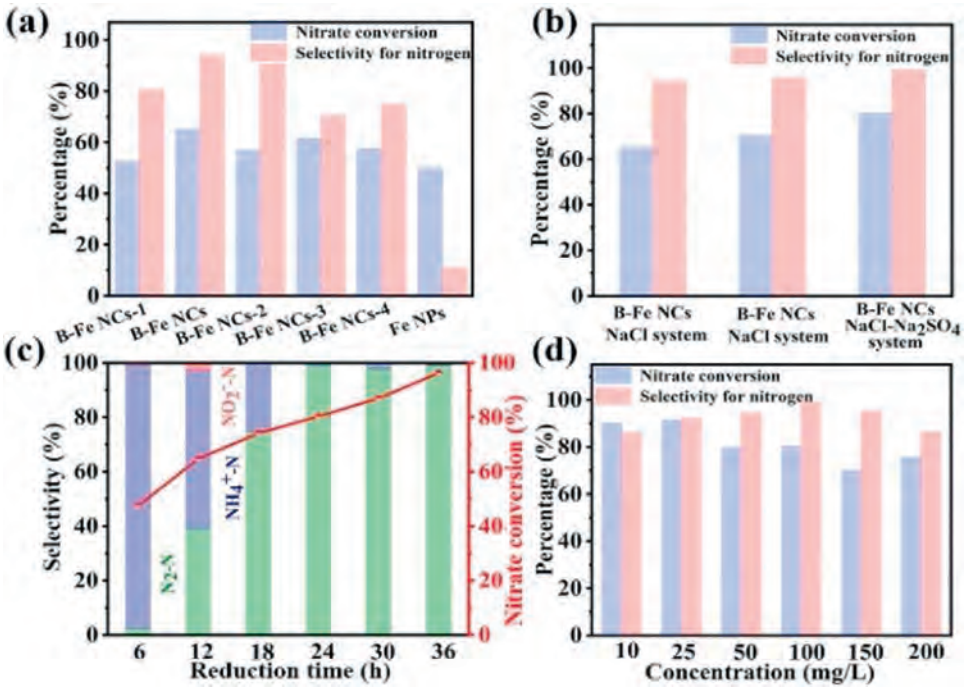

Fig. 3. (a) Nitrate conversion and nitrogen selectivity of B-Fe NCs-x and Fe NPs cathodes in 0.02 mol/L NaCl electrolyte containing 100 mg/L NO_3^--N at −1.3 V applied potential for 24 h. (b) Nitrate conversion and nitrogen selectivity of the B-Fe NCs with different conditions (The two leftmost columns: the deionized water without deoxidized; The middle two columns and the two rightmost columns: the deionized water with deoxidized). (c) Nitrate conversion and nitrogen selectivity of B-Fe NCs result along with time in 0.02 mol/L NaCl and 0.02 mol/L Na_2SO_4 containing 100 mg/L NO_3^--N at −1.3 V applied potential. (d) Effects of initial nitrate concentrations in 0.02 mol/L NaCl and 0.02 mol/L Na_2SO_4 mixed electrolyte at −1.3 V applied potential for 24 h.

activity, the optimal mixed electrolyte system was determined to be 0.02 mol/L Cl^- and 0.02 mol/L SO_4^{2-}.

An optimal applied potential is also the critical factor to effectively catalyze nitrate reduction to avoid harmful by-products. Therefore, electrocatalysis tests were carried out at different applied potentials. As shown in Fig. S7b (Supporting information), the optimal applied potential of B-Fe NCs is −1.3 V. In order to further evaluate the optimum applied potential, the current efficiency of cathodic nitrate reduction at different cathode potentials was calculated by the following Eq. 1:

$$EC\ \% = \frac{nFV\Delta C_{exp}}{Q} \times 100\% \quad (1)$$

ΔC_{exp} (mol/L) is the concentration change of NO_3^- after electrocatalysis. Fig. S8a (Supporting information) shows a few representative current densities of B-Fe NCs cathode at varied applied potentials. Fig. S8b (Supporting information) illustrates the electronic current efficiency at different current densities. The results show that the B-Fe NCs cathode can obtain better utilization efficiency at lower potential, but considering its electrocatalytic activity (nitrate conversion and nitrogen selectivity), the best application potential is still -1.3 V.

The electrocatalytic performance of B-Fe NCs in 0.02 mol/L NaCl and 0.02 mol/L Na_2SO_4 electrolyte containing different concentration of NO_3^--N has been evaluated in Fig. 3d. In the relative low nitrate concentration (10 and 25 mg/L NO_3^--N), B-Fe NCs still exhibits excellent nitrate conversion (> 90%) and nitrogen selectivity (> 86%). When the nitrate concentration was higher than 100 mg/L, the nitrate conversion and nitrogen selectivity undesirably decreased, suggesting the fully occupied active sites by pollutant molecules cannot further play the role of nitrate conversion.

In addition, the evaluation of electrocatalytic denitrification in real water is of great significance for the practical application of catalysts. As shown in Fig. S9 (Supporting information), the original lake water was cleared by suction filtration treatment. Subsequently, since the nitrate concentration in the initial lake water was lower than 5 mg/L, purified lake water was used to prepare the electrolyte solutions of 10 and 100 mg/L. The result showed that the nitrate conversion was 44% and 54%, and nitrogen selectivity was 72% and 83%, respectively. It is worth noting that the composition of actual water is complex, including heavy metals, inorganic anions, organic matter and unknown ion concentration, which would lead to the degradation of catalyst performance in practical application.

The cycle experiments of B-Fe NCs were used to evaluate the stability of catalyst for NRR. As shown in Fig. 4a, the conversion of nitrate varies from 80% to 90% and the nitrogen selectivity is more than 88% after 20 cycles, indicating the excellent catalytic stability. To estimate the structural variation of the catalyst after the NRR for 24 h, XRD and TEM were used to characterize the structure of the B-Fe NCs after electrocatalysis for 24 h. Furthermore, the corrosion and leaching of iron ions after long time electrolysis were determined by ICP-MS. After 20 cycles, the iron leaching amount accounts for 4.1% of the total iron mass (Fig. 4b). At the same time, the crystallographic information of nickel foam loaded B-Fe NCs before and after NRR are shown in Fig. 4c, suggesting that the crystal structure of B-Fe NCs maintained well after NRR. TEM image in Fig. 4d shows that the catalyst still retains the core-shell structure, demonstrating the structural stability of B-Fe NCs [48].

Reaction mechanism of B-Fe NCs for NRR is shown in the Fig. 5. The electroreduction of nitrate includes a “rate-determining step” and a “selectivity determining step” [29]. Electrocatalytic nitrate reduction begins with the adsorption of nitrate on the electrode surface. Then, the adsorbed nitrate is reduced to nitrite by gaining electrons, which is the “rate-determining step” of the nitrate reduction reaction. It is reported that the significant hybridization between B 2p state and the metal 3d orbit is accompanied by the concentration of charges between metal-boron (M—B) and boron-boron (B—B), and the weakening of metal-metal (M—M) bond,

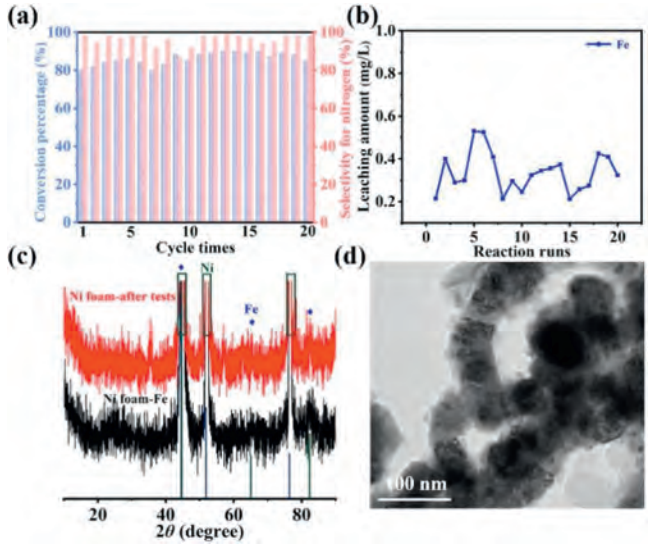

Fig. 4. (a) Nitrate conversion and nitrogen selectivity recorded over 20 times repeated electrolysis tests (each test lasting 24 h). (b) Iron leaching amount of the B-Fe NCs cathode during 20 repeated electrolysis tests. (c) XRD pattern of B-Fe NCs after electrocatalytic reaction in 0.02 mol/L NaCl and 0.02 mol/L Na_2SO_4 electrolyte containing 100 mg/L NO_3^--N for 24 h (The red line represents nickel foam loaded B-Fe NCs after test, the black line represents nickel foam loaded B-Fe NCs before test). (d) TEM image of B-Fe NCs after electrocatalytic reaction in 0.02 mol/L NaCl and 0.02 mol/L Na_2SO_4 solution containing 100 mg/L NO_3^--N for 24 h.

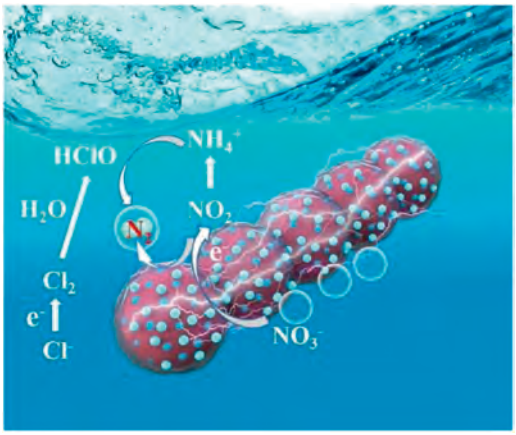

Fig. 5. Reaction mechanism of B-Fe NCs for nitrate reduction.

which will be beneficial to reduce the energy barrier of intermediate formation in the catalytic process [33,40,41,49]. Based on this, it can be inferred that B-Fe NCs is beneficial to the nitrate adsorption in this step. The well-crosslinked chain-like architectures can provide ample accessible channels for electronic transmission. At the selectivity-determining step, nitrite (NO_2^-) rapidly gains electrons to generate intermediate NO, and then continuously generates intermediate N_2O by the hydrogen reduction, further converting into N_2 and NH_4^+. Ammonia can be inevitably produced due to the direct reduction of aqueous NO_2^- and strongly surface bonded NO [45]. It is worth noting that the existence of chloride ions in electrolyte is beneficial to improve the selectivity of nitrogen in nitrate reduction products of iron-based catalysts [25]. In the reaction process, Cl^- adsorbed on the anode surface can obtain electrons to generate intermediate HClO, and NH_4^+ generated by catalytic reaction can diffuse to the anode surface to further react with HClO in the system to generate N_2. This speculation is consistent with the time distribution of reduction products. In order to highlight the advantages of this structure, the B-Fe NCs and several other NRR cathodes were compared. The results of nitrate conversion and nitrogen selectivity of these cathodes were summarized in Table S2 (Supporting information). Compared with CuPb@OMC [50], Ag@carbon [18], CL-Fe@C [25], Fe/Fe_3C-NCNF [26], nZVI@OMC [46], Fe@C [51], Cu-Pd/NZVI [52], and CuPb@coralline-like NC [22], the B-Fe NCs catalyst exhibits outstanding nitrate conversion and nitrogen selectivity.

In summary, the B-Fe NCs-x with adjustable Fe/B ratio have been synthesized *via* a precipitation of metal cations by $NaBH_4$. The doped heteroatom (B) plays an important role in regulating electronic density for the Fe atom for improving the NRR catalytic performance. In addition, the well-crosslinked chain-like architectures benefit the mass/electron transport to boost the exposure of catalytic active sites. These features endow the B-Fe NCs with excellent nitrate conversion of 80% and the ultra-high nitrogen selectivity of 99%. It is believed that this study may open a way to explore efficient and low-cost metal boride catalysts for NRR.

Declaration of competing interest

The authors report no declarations of interest.

Acknowledgments

This work was financially supported by the Fok Ying-Tong Education Foundation (No. 171041), Shanghai Scientific and Technological Innovation Project (No. 19JC1410400), Program for Professor of Special Appointment (Eastern Scholar) at Shanghai Institutions of Higher Learning, and State Key Laboratory for Modification of Chemical Fibers and Polymer Materials, Donghua University.

Appendix A. Supplementary data

Supplementary material related to this article can be found, in the online version, at doi:https://doi.org/10.1016/j.cclet.2021.03.042.

References

[1] M. Duca, M.T.M. Koper, Energy Environ. Sci. 5 (2012) 9726–9742.
[2] F. Liu, Y. Yu, H. He, Chem. Commun. 50 (2014) 8445–8463.
[3] S. Ghafari, M. Hasan, M.K. Aroua, Bioresour. Technol. 99 (2008) 3965–3974.
[4] X. Guan, Y. Sun, H. Qin, et al., Water Res. 75 (2015) 224–248.
[5] M. Sebilo, G. Aloisi, B. Mayer, et al., Sci. Rep. 9 (2019) 19206.
[6] P. Clauwaert, K. Rabaey, P. Aelterman, et al., Environ. Sci. Technol. 41 (2007) 3354–3360.
[7] M. Alikhani, M.R. Moghbeli, Chem. Eng. J. 239 (2014) 93–104.
[8] L.J. Banasiak, A.I. Schäfer, J. Membr. Sci. 334 (2009) 101–109.
[9] R. Epsztein, O. Nir, O. Lahav, M. Green, Chem. Eng. J. 279 (2015) 372–378.
[10] J. Gao, B. Jiang, C. Ni, et al., Appl. Catal. B 254 (2019) 391–402.
[11] H. Xu, J. Wu, W. Luo, et al., Small 16 (2020) 2001775.
[12] X. Zhang, Y. Wang, C. Liu, et al., Chem. Eng. J. 403 (2021) 126269.
[13] X. Wang, M. Zhu, G. Zeng, et al., Nanoscale 12 (2020) 9385–9391.
[14] R. Jia, Y. Wang, C. Wang, et al., ACS Catal. 10 (2020) 3533–3540.
[15] M. Kuang, P. Han, L. Huang, et al., Adv. Funct. Mater. 28 (2018) 1804886.
[16] Y.J. Sa, C.W. Lee, S.Y. Lee, et al., Chem. Soc. Rev. 49 (2020) 6632–6665.
[17] M. Cattelan, G.W. Peng, E. Cavaliere, et al., Nanoscale 7 (2015) 2450–2460.
[18] J. Liu, T. Cheng, L. Jiang, A. Kong, Y. Shan, ACS Appl. Mater. Interfaces 12 (2020) 33186–33195.
[19] M. Duca, B. van der Klugt, M.A. Hasnat, M. Machida, M.T.M. Koper, J. Catal. 275 (2010) 61–69.
[20] S. Seraj, P. Kunal, H. Li, et al., ACS Catal. 7 (2017) 3268–3276.
[21] J. Wang, W. Teng, L. Ling, et al., Environ. Sci. Nano 7 (2020) 1496–1506.
[22] M. Chen, H. Wang, Y. Zhao, et al., Nanoscale 10 (2018) 19023–19030.
[23] F. Liang, J. Fan, Y. Guo, et al., Ind. Eng. Chem. Res. 47 (2008) 8550–8554.
[24] Q. Wang, W. Luo, X. Chen, et al., Chem. Eur. J. 24 (2018) 15663–15668.
[25] L. Su, D. Han, G. Zhu, et al., Nano Lett. 19 (2019) 5423–5430.
[26] Y. Lan, J. Chen, H. Zhang, W.X. Zhang, J. Yang, J. Mater. Chem. A 8 (2020) 15853–15863.
[27] J. Wang, L. Ling, Z. Deng, W.X. Zhang, Sci. Bull. 65 (2020) 926–933.
[28] W. Li, C. Xiao, Y. Zhao, et al., Catal. Lett. 146 (2016) 2585–2595.

[29] W. Xu, Y. Bai, Y. Yin, Adv. Mater. 30 (2018) 1802091.
[30] L. Su, J. Ma, J. Wang, et al., Chem. Commun. 56 (2020) 2795–2798.
[31] H. Xu, H. Xu, Z. Chen, et al., ACS Appl. Mater. Interfaces 11 (2019) 3861–3868.
[32] L. Jiao, W. Xu, Y. Zhang, et al., Nano Today 35 (2020) 100971.
[33] H. Ren, X. Sun, C. Du, et al., ACS Nano 13 (2019) 12969–12979.
[34] L. Chen, L.R. Zhang, L.Y. Yao, et al., Energy Environ. Sci. 12 (2019) 3099–3105.
[35] K. Deng, T. Ren, Y. Xu, et al., J. Mater. Chem. A 8 (2020) 5595–5600.
[36] Y. Zhou, F. Che, M. Liu, et al., Nat. Chem. 10 (2018) 974–980.
[37] S.R. Kanel, J.-M. Grenèche, H. Choi, Environ. Sci. Technol. 40 (2006) 2045–2050.
[38] Y. Yang, L. Zhuang, R. Lin, et al., J. Power Sources 349 (2017) 68–74.
[39] X. Zhou, D. Xu, Y. Chen, Y. Hu, Chem. Eng. J. 384 (2020) 123324.
[40] J. Masa, I. Sinev, H. Mistry, et al., Adv. Energy Mater. 7 (2017) 1700381.
[41] Q. Liu, H. Zhao, M. Jiang, et al., J. Mater. Chem. A 8 (2020) 13638–13645.
[42] H. Sun, X. Xu, Z. Yan, et al., J. Mater. Chem. A 6 (2018) 22062–22069.
[43] S. Zheng, S. Li, Z. Mei, et al., J. Phys. Chem. Lett. 10 (2019) 6984–6989.
[44] S.L. Candelaria, N.M. Bedford, T.J. Woehl, et al., ACS Catal. 7 (2017) 365–379.
[45] W. Duan, G. Li, Z. Lei, et al., Water Res. 161 (2019) 126–135.
[46] W. Teng, N. Bai, Y. Liu, et al., Environ. Sci. Technol. 52 (2018) 230–236.
[47] K. Sohn, S.W. Kang, S. Ahn, M. Woo, S.K. Yang, Environ. Sci. Technol. 40 (2006) 5514–5519.
[48] J. Liu, Y. Ji, J. Nai, et al., Energy Environ. Sci. 11 (2018) 1736–1741.
[49] J. Masa, P. Weide, D. Peeters, et al., Adv. Energy Mater. 6 (2016) 1502313.
[50] J. Fan, H. Xu, M. Lv, et al., New J. Chem. 41 (2017) 2349–2357.
[51] W. Hong, L. Su, J. Wang, et al., Chem. Commun. 56 (2020) 14685–14688.
[52] S. Hamid, S. Bae, W. Lee, M.T. Amin, A.A. Alazba, Ind. Eng. Chem. Res. 54 (2015) 6247–6257.